# Durability of nanostructured LaPrNiO4+δ electrode for solid oxide cells: Electrochemical, microstructural, and structural investigation

Nur Istiqomah Khamidy, Jérôme Laurencin, Dario Ferreira Sanchez, Federico Monaco, Frédéric Charlot, Elisabeth Djurado

HAL Id: hal-02464568

https://hal.univ-grenoble-alpes.fr/hal-02464568v1

Submitted on 21 Jul 2022

# Durability of nanostructured LaPrNiO$_{4+\delta}$ electrode for solid oxide cells: electrochemical, microstructural, and structural investigation

Nur Istiqomah Khamidy[a], Jérôme Laurencin[b*], Dario Ferreira Sanchez[c], Federico Monaco[b], Frederic Charlot[d], and Elisabeth Djurado[a]

[a]Univ. Grenoble Alpes, Univ. Savoie Mont Blanc, CNRS, Grenoble INP, LEPMI, 38000 Grenoble, France

[b]Univ. Grenoble Alpes, CEA/LITEN, 17 rue des Martyrs, F-38054 Grenoble, France

[c] Swiss Light Source, Paul Scherrer Institut, CH-5232 Villigen PSI, Switzerland

[d]CMTC, Grenoble INP, Univ. Grenoble Alpes, F-38000, France

*Corresponding author*: Jérôme Laurencin

E-mail: jerome.laurencin@cea.fr, Tel: +33- 438782210; Fax: +33-438783589

**Abstract:**

This work reports a durability study in galvanostatic mode at 700 °C for 900-960 h related to structural and microstructural evolution of LaPrNiO$_{4+\delta}$ (LPNO) oxygen electrode. The performances of the electrode, deposited by electrostatic spray deposition (ESD) and screen printing (SP), are not changed when operated under electrolysis current whereas a degradation is observed in fuel cell mode. Small quantities of secondary phases (La,Pr)$_3$Ni$_2$O$_{7-\delta}$ in the fine ESD microstructure and Pr$_6$O$_{11}$ on both ESD and SP layers are detected in the pristine electrode by synchrotron μ-X-ray diffraction and fluorescence. The destabilization of LPNO electrode, which slightly occurs in the ESD layer after thermal aging in air, is strongly accelerated under anodic and cathodic currents. Indeed, the formation of a new phase (La,Pr)$_4$Ni$_3$O$_{10-\delta}$ on both ESD and SP layers occurs with the extension of (La,Pr)$_3$Ni$_2$O$_{7-\delta}$ in the SP layer, and a significant increase in the amount Pr$_6$O$_{11}$ at high current density. Nevertheless, the electrode microstructure, determined by FIB-SEM tomography, remains stable under current whereas severe delamination is observed after aging in fuel cell mode. Based on these characterizations, the mechanisms of electrode aging have been discussed to explain the different behavior in fuel cell and electrolysis modes.

# 1. Introduction

Solid oxide cell (SOC) is an energy conversion system which can operate reversibly on fuel cell and electrolysis modes. It normally operates at a temperature as high as 900 °C and it is of current interest to reduce the operating temperature due to several issues especially on material selection, cost, and durability [1–3]. Lanthanum-praseodymium nickelates $La_{2-x}Pr_xNiO_{4+\delta}$ ($0 \leq x \leq 2$) is one of the most suitable and promising materials used as oxygen electrode for intermediate temperature solid oxide cells (IT-SOC; operates at a temperature around 650-750 °C) [4,5]. This material is a mixed ionic-electronic conductor (MIEC) based on the $K_2NiF_4$ structure and belongs to the Ruddlesden-Popper phase which has a general formula of $A_{n+1}B_nO_{3n+1}$. Indeed, MIECs allow the incorporation of oxygen ions into the lattice and diffusion through the material, thus expanding the electrochemically active surface area within the cathode, extending the oxygen reduction reaction (ORR) beyond the triple-phase boundary (TPB) lines, and, as a result, increasing overall performance. The oxygen over stoichiometry of this structure, which presents $O^{2-}$ ions in the interstitial sites, provides the oxygen transport properties in the bulk material [6]. It has been reported that besides having good ionic transport properties, lanthanum-praseodymium nickelate compounds also show good electronic conductivity (~80 to 100 S cm$^{-1}$) due to the metal mixed-valence [7,8]. The oxygen transport properties, electrochemical activity, and chemical stability of lanthanum-praseodymium nickelates depend on the amount of praseodymium in the compound. $Pr_2NiO_{4+\delta}$ presents higher diffusivity of oxide ions and surface exchange coefficients than $La_2NiO_{4+\delta}$ [9,10]. Therefore, the praseodymium-rich nickelate results in higher electrochemical activity compared to the lanthanum-rich nickelate [7,11]. However, the chemical stability of the former is less than the one of lanthanum-rich nickelate. A set of studies by Montenegro-Hernández, *et. al.*, showed that $La_2NiO_{4+\delta}$ (LNO) was chemically stable while $Pr_2NiO_{4+\delta}$ (PNO) decomposed into $Pr_6O_{11}$ after thermal aging on powders at 700 °C for at least 24 h [12]. Another study on powders of $La_{2-x}Pr_xNiO_{4+\delta}$ ($x$ = 0, 0.5, 1, 1.5, 2) by Vibhu, *et. al*, showed that the stoichiometry with $x$ = 0 and 0.5 were stable while the praseodymium-rich phases ($1 \leq x \leq 2$) decomposed into $(La,Pr)NiO_3$, $(La,Pr)_4Ni_3O_{10-\delta}$, and $Pr_6O_{11}$ [13]. It

was also shown that the thermal destabilization of the nickelate phase is favored with the increasing of praseodymium content. Sharma, *et. al*, reported thermal aging study at 700 °C for 30 days for La$_{2-x}$Pr$_x$NiO$_{4+\delta}$ ($x$ = 0, 0.5, 1, 2) deposited by electrostatic spray deposition (ESD) on gadolinium-doped ceria (GDC) electrolyte [14]. The investigations showed that the compounds were thermally stable up to $x$ = 1, while the praseodymium nickelate ($x$ = 2) decomposed into PrNiO$_3$, Pr$_6$O$_{11}$, and NiO. Long-term tests for 500 h were also reported in the study for the compound with $x$ = 1 and showed that the electrochemical performance was stable at 700 °C with no applied current. The difference between the decomposition products in these aforementioned works can be attributed to the different electrode microstructures. Thus, in order to have a trade-off between the electrochemical performance and the chemical stability, as well as by considering the preparation technique by ESD, a lanthanum-praseodymium nickelate stoichiometry with $x$ = 1, LaPrNiO$_{4+\delta}$ (LPNO), is chosen as the material in this study.

In a previous work [15], the electrochemical performance of LPNO electrode has been improved by varying the design and microstructure of the electrode by combining electrostatic spray deposition (ESD) for the active functional layer (AFL) and screen printing (SP) for the current collector. A decrease in the polarization resistance (R$_{pol}$) was measured from 0.72, 0.63 down to 0.50 Ω cm$^2$ at 600 °C when the LPNO electrode was designed as a single layer by ESD, SP, and as a double-layer consisting of ESD topped by SP, respectively. The performance of the innovative double-layer architecture of the electrode has been optimized thanks to an improvement of the flat current collecting layer (CCL) surface and of the electrode/electrolyte interface with the presence of more electrochemically active particles at the nanometer-length scale. Moreover, this AFL of coral-type morphology deposited by ESD presents high crystallinity and good adhesion to the electrolyte at a low sintering temperature (960 °C). Thus, in this work, an aging study based on this innovative LPNO architecture oxygen electrode is proposed since much of the most exciting recent research involves developing new means of controlling the structure at the electrolyte/electrode interface, which is the critical region determining the performance and lifetime of solid oxide electrochemical cells [16-19]. It is worth noting that the presence of a secondary phase of

higher-order nickelate (La,Pr)$_3$Ni$_2$O$_{7-\delta}$, (LP)3N2, was detected on the active layer of the pristine electrode prepared by ESD. The formation of the secondary phase is likely due to the coral-like microstructure of the ESD layer which exhibits an open microstructure with large porosities and small particle size in the nanometric scale. This very fine microstructure is suspected to be more reactive than the coarser microstructure of the layer prepared by SP. The (LP)3N2 is also an electrochemically active material which can improve the electrochemical activity of the electrode [20-22]. However, the presence of this secondary phase, combined with the nature of the microstructure, might affect the chemical stability of the electrode. In this study, several electrodes have been prepared and then subjected to several long-term tests in both symmetrical and complete cells, with and without polarization in electrolysis and fuel cell modes. In order to analyze the durability experiments and to investigate the LPNO stability, the tested electrodes have been characterized using several techniques. The electrode microstructure has been observed by scanning electron microscopy (SEM) and reconstructed by FIB-SEM tomography. In complementarity, structural characterizations have been performed by using laboratory X-ray diffraction together with synchrotron µ-X-ray diffraction (µ-XRD) and µ-X-ray fluorescence (µ-XRF).

## 2. Experimental

### 2.1. Samples preparation

The LPNO oxygen electrodes were deposited by electrostatic spray deposition (ESD) and screen printing (SP). ESD is a technique based on the electrohydrodynamic law in which a precursor solution is injected through a needle that is directed towards a heated and grounded substrate [23]. The precursor solution was prepared from the precursor powders of La(NO$_3$)$_3$.6H$_2$O (Acros Organic, 98.00 %), Pr(NO$_3$)$_3$.6H$_2$O (Sigma-Aldrich 99.90 %), and Ni(NO$_3$)$_2$.6H$_2$O (Fischer Scientific, 99.00 %) in stoichiometric ratio, as well as 30 mol. % excess of citric acid C$_6$H$_8$O$_7$ (Acros Organic, 99.5 %) as the chelating agent. These powders were dissolved in a mixture of absolute ethanol (C$_2$H$_5$OH or EtOH, VWR Chemical, 99.95%)

and $H_2O$ (1:2) in 0.02 M (total cation concentration). To stabilize the solution and prevent the formation of precipitates in the solution, 8 drops of nitric acid ($HNO_3$, Chem-Lab, 65% vol.) were added for 30 mL of solution. Based on previous work [24], specific deposition parameters detailed hereafter are selected to obtain the coral-like microstructure: temperature of 350 °C, a needle-to-substrate distance of 50 mm, a solution flow rate of 1.5 mL $h^{-1}$, and a deposition time of 4.5 hours. During the ESD deposition, the voltage was fixed to approximately 12-14 kV. The sintering after ESD deposition was carried out at 960 °C for 6 hours in the air to promote crystallization and phase formation.

The LPNO powder for SP was prepared in the lab by an auto-combustion technique by using the same precursor powders like the ones to prepare ESD precursor solution. The stoichiometric amounts of the nitrates and 30 mol. % excess of citric acid were dissolved in absolute ethanol in 0.02 M (total cation concentration). This solution was then heated at around 120 °C while maintaining the stirring until gel-like precipitates were formed. The precipitates were manually ground and sintered in air subsequently at 1050 °C for 2 h and at 1100 °C for 0.5 h. The post-sintered powder was manually ground and was then ball-milled using a planetary ball mill for 2 h to obtain fine LPNO powder. The ink for SP was prepared by mixing LPNO powder and organic solvent (KD2921, Zschimmer, and Schwarz) with the mass ratio of 1:1, and an addition of 1 wt. % polyvinyl butyral ($(C_8H_{14}O_2)_n$, Aldrich) as a binder. This mixture was stirred and then passed through the three-roll mill to further blend and homogenize the ink. The ink was then used for screen printing. The deposited SP layer was then sintered in the air firstly at 450 °C for 2 h to remove the organic solvent followed by sintering at 800 °C for 2 h.

Two types of electrode configurations were prepared for this study. The first one was called a single layer (SL) electrode which consists of an active functional layer (AFL) of LPNO deposited by ESD. The second configuration was a double layer (DL) electrode in which an AFL of LPNO was firstly deposited on the electrolyte by ESD which was then topped by the current collector layer (CCL) of LPNO deposited by SP. The layer was sintered after each deposition under the conditions mentioned previously for each technique.

The pristine electrode, thermally-aged electrode, and symmetrical cell (see **Table 1**) were prepared by depositing LPNO on top of gadolinium-doped ceria ($Ce_{0.9}Gd_{0.1}O_{2-\delta}$, GDC) thick electrolyte used as cell support. The dense GDC pellets, 1.1 mm thick and 19.6 mm in diameter, were prepared by pressing commercial powder (Praxair) followed by sintering at 1400 $^\circ$C for 4 h in air. The complete cell (see **Table 1**) was prepared by depositing LPNO on top of a commercial half-cell. The half-cell, which is 50 mm in diameter and 250 µm-thick, consists of a thin (~8 µm) 8 mol% yttria-stabilized zirconia (8YSZ) electrolyte deposited on top of thick cermet Ni-YSZ as the hydrogen electrode. A 4 µm thin GDC barrier layer was deposited on top of the YSZ electrolyte to prevent a reaction between LPNO electrode and YSZ electrolyte. The LPNO oxygen electrode, 20 mm in diameter, is then deposited on top of this GDC barrier layer.

**Table 1** List of samples and the summary of the characterization results.

| | | Pristine electrode (reference) | Thermally-aged electrode | Long-term test in electrolysis mode | | Long-term test in fuel cell mode |
|---|---|---|---|---|---|---|
| **Samples** | | Sample 1 | Sample 2 | Sample 3 (symmetrical cell) | Sample 4 (complete cell) | Sample 5 (symmetrical cell) |
| **Configuration** | | DL on GDC electrolyte | SL ESD on GDC electrolyte | DL on GDC electrolyte | DL on half-cell GDC/YSZ/Ni-YSZ | DL on GDC electrolyte |
| **Treatment** | | N/A (as-prepared sample) | 700 °C, 1000 h in air | 700 °C, 960 h in air, at +300 mA cm$^{-2}$ | 700 °C, 900 h in 90/10 $H_2O/H_2$, at +200 mA cm$^{-2}$ | 700 °C, 960 h in air, at -300 mA cm$^{-2}$ |
| **Microstructures** | | No delamination | No delamination | No delamination | No delamination | Delamination of LPNO electrode from GDC electrolyte |
| **Lab XRD** | **ESD layer** | LPNO + (LP)3N2 | Not available (N/A) | N/A | N/A | Bulk electrode: LPNO + (LP)3N2 + $Pr_6O_{11}$ + (LP)4N3 |
| | **SP layer** | LPNO | N/A | N/A | N/A | |
| **µ-XRD and µ-XRF** | **ESD layer** | LPNO + (LP)3N2 + $Pr_6O_{11}$ | LPNO + (LP)3N2 + $Pr_6O_{11}$ | LPNO + (LP)3N2 + $Pr_6O_{11}$ + (LP)4N3 | LPNO + (LP)3N2 + $Pr_6O_{11}$ + (LP)4N3 | N/A |
| | **SP layer** | LPNO + $Pr_6O_{11}$ | N/A | LPNO + (LP)3N2 + $Pr_6O_{11}$ + (LP)4N3 | LPNO + (LP)3N2 + $Pr_6O_{11}$ + (LP)4N3 | N/A |

## 2.2. Aging of the cells

The samples studied in this work have been listed in **Table 1**. The first type of the sample, which was used as the reference for the study, was the pristine electrode with no aging treatment (sample 1). Three different pristine electrodes deposited on a side of GDC pellet were prepared: two single layer LPNO electrodes deposited either by ESD (27 μm-thick) or SP (25 μm-thick), and a double layer electrode (38 μm-thick). The first two samples were used for characterization by laboratory X-ray diffraction and the third one was used for synchrotron μ-X-ray diffraction and μ-X-ray fluorescence (see §2.5 for more details on both characterization techniques). The second type of the sample was a single layer LPNO deposited by ESD on a side of GDC pellet which was then thermally aged at 700 °C in the air for 1000 h (sample 2). The third type of the sample was a symmetrical cell in which double-layer LPNO, 10 mm in diameter, was deposited on both sides of GDC pellet (samples 3 and 5). For the purpose of electrochemical measurement by a 3-electrode configuration, a silver wire was placed approximately in the middle of the side of GDC electrolyte pellet as the reference electrode. Gold grids (Heraeus, 1024 meshes cm$^{-2}$ woven from 0.06 mm in diameter wire) were used as current collectors. This sample was then subjected to a long-term electrochemical characterization at 700 °C for 960 h in the air using autolab potentiostat-galvanostat (PGSTAT 302N). During the long-term experiment, DC polarization currents ($i_{dc}$) of +300 mA cm$^{-2}$ and -300 mA cm$^{-2}$ were applied on the upper and lower electrode, respectively. It means that the upper electrode was subjected to an anodic polarization and worked in electrolysis mode (sample 3), while the lower electrode was under a cathodic polarization and fuel cell mode (sample 5). Before and after the long term study, electrochemical impedance spectroscopy (EIS) was carried out on each side of the electrode at the open circuit potential (OCP) in galvanostatic mode with a sinusoidal amplitude of 10 mA in the 0.01 Hz - 1MHz frequency range. The last type of the sample was the complete cell in which double-layer LPNO was deposited on top of the GDC barrier layer on YSZ electrolyte (sample 4). Nickel grid (50 mm in diameter) and gold grid (34 mm in diameter) were used as the current collector on the hydrogen electrode and oxygen electrode, respectively. To ensure gas tightness between both sides of the cell, glass sealing was carried out at 860 °C for 1.5 h. A load of 3.38

kg ($\approx$ 0.37 kg cm$^{-2}$) was applied to ensure good contact between the cell and the current collector grids. Before the electrochemical measurement, the NiO on the hydrogen electrode was first reduced to Ni. The NiO reduction was carried out by passing a mixture of $N_2$ and $H_2$ gases with a total flow rate of 4 Nl/h to the hydrogen electrode side; the reduction started with pure $N_2$, followed by increasing the amount of $H_2$, and the last step was with pure $H_2$. Air was passed on the oxygen electrode side with a flow rate of 4 Nl/h during the reduction. The cell was then operated under electrolysis mode under current of 200 mA cm$^{-2}$. A flux of 1.456 Nl h$^{-1}$ of $H_2$ and 0.655 Nl h$^{-1}$ of $O_2$ was used to achieve the $H_2O/H_2$ ratio of 90/10 and steam conversion rate of 20%. The electrochemical characterization was carried out at 700 °C for 900 h and the potential was recorded over time. As in the symmetrical cell previously discussed, EIS was also performed before and after the long-term aging.

In the reported results, all the EIS diagrams had been normalized by the surface area (S) of the electrodes, which are 0.79 cm$^2$ and 3.14 cm$^2$ for symmetrical and complete cells, respectively. The polarization resistance ($R_{pol}$) value, which was used to quantify the electrode performances, is defined as:

$$R_{pol} = R_{electrode} \times S \qquad \text{(Eq. 1)}$$

where S is the surface area of the electrode. The term $R_{electrode}$ was deduced from impedance plotted in the Nyquist representation by measuring the difference between the low (LF) and high frequency (HF) intercepts with the real axis. In addition, series resistance ($R_s$) was also extracted from the Nyquist plot which is equal to the high frequency (HF) intercept with the real axis.

## 2.3. Microstructural characterization

The morphology of the films was analyzed by scanning electron microscopy (SEM, ZEISS Ultra 55 instrument with a field emission gun, FEG). The average particle size was estimated from the SEM images by using ImageJ software.

The 3D reconstructions of two selected electrodes (sample 1 and sample 3 in **Table 1**) were obtained by focused ion beam (FIB)-SEM using either Crossbeam 550 (ZEISS) and Crossbeam NVision 40 (ZEISS, with a specific FIB column from SEYCO SII) machines. Gallium source was used to produce $Ga^+$ ions for the milling. The voxel size of each slice of the image was 15 x 15 x 15 nm. The slices of the images from FIB-SEM were then stacked into a 3D volume and segmented by using Atlas3D (Fibics) and Fiji (ImageJ) software. The microstructural properties of the two electrodes (e.g. the porosity, specific surface area, tortuosity and particle size distribution (PSD)) were computed on the reconstructions by using in-house MATLAB codes [25].

## 2.4. Lamellae preparation for µ-XRD and µ-XRF characterization

For the purpose of characterization by µ-X-ray diffraction and µ-X-ray fluorescence, thin lamellae were extracted from the samples after their respective aging treatment by using a plasma-focused ion beam (p-FIB) Vion (FEITM) machine working with an inductively coupled plasma ions source. This technology uses $Xe^+$ ions allowing higher maximum currents and milling rates about 60 times faster than classical $Ga^+$ FIB [26]. The lamellae were prepared by firstly positioning the samples in the vacuum chamber of the plasma-FIB machine on a five-axial motorized stage. After the identification of the eucentric height, the region of interest (ROI) was covered with a Platinum (Pt) deposition (~3-4 µm) to protect the samples surfaces (**Fig. 1a**) using a low current of 15 nA [27]. Subsequently, the two sides of the ROI were milled to obtain the lamella in the sample (**Fig. 1b**). This step was performed at two currents, 180 nA and 59 nA, far and close to the ROI, respectively. Once the milling was completed (**Fig. 1c**), a small Pt deposition was used to fix it on a specific micromanipulator and the sample was detached from the cell using a low ion current of 59 nA (**Fig. 1d**). Finally, the last Pt deposition was used to glue the lamella detached from the cell to an aluminum pin-compatible with the sample holder of the beamline (**Fig. 1e**). The extracted lamellae dimensions were approximately 100 x 80 x 20 µm³ (for width, height, and depth respectively) as illustrated in the SEM images provided in **Fig. S1**.
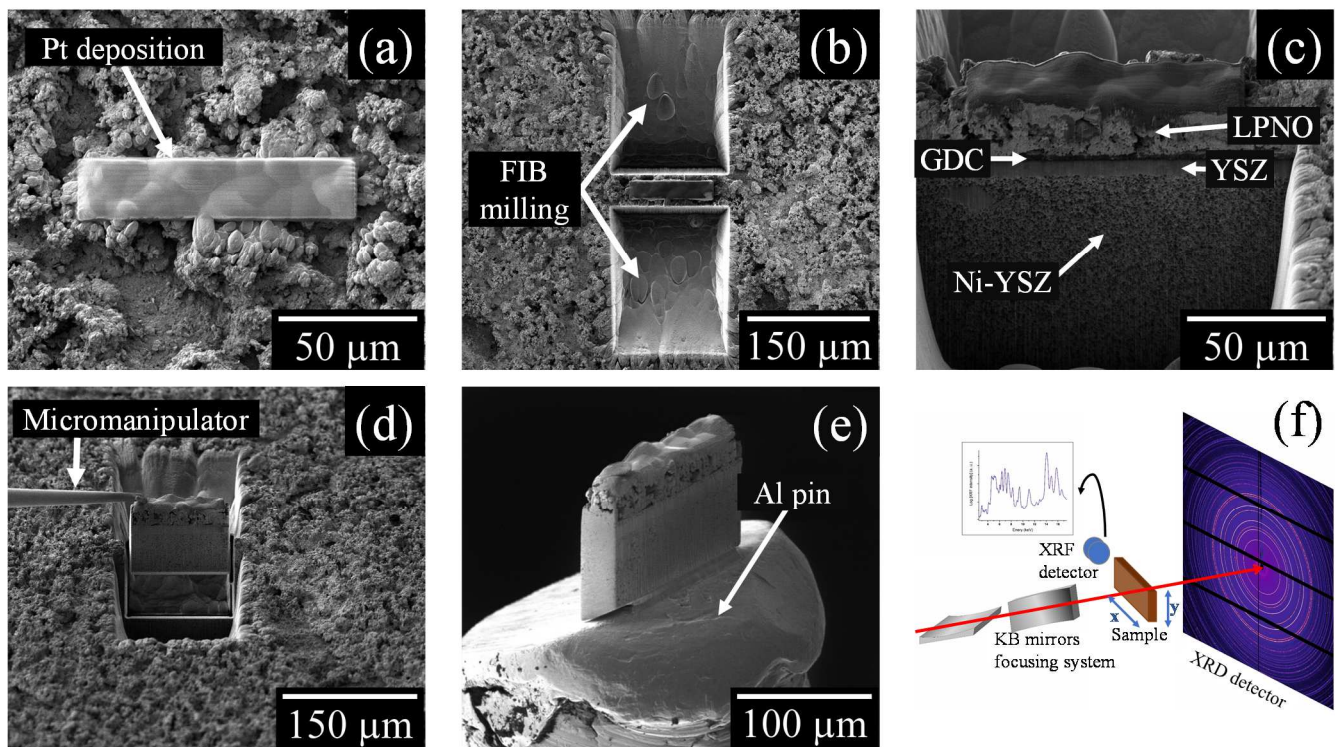
**Fig. 1** Schematic representation of the sample preparation technique (example given for the sample coming from the complete cell): (a) protective Pt deposition on ROI – (b) FIB milling around the ROI – (c) isolated lamella – (d) sample extraction from the cell – (e) sample mounted on the Al pin. (f) The schematic diagram of μ-XRD and μ-XRF characterization at μXAS beamline, SLS, PSI, Switzerland.

## 2.5. Structural characterization

The structural characterization of two selected cells (sample 1 prepared by ESD and SP) was carried out with a laboratory setup X-ray diffraction (XRD, PANalytical X'pert Pro MPD, Cu Kα radiation, $\lambda$=1.5419 Å) in Bragg-Brentano geometry. The phases were identified based on the powder diffraction file (PDF) from the International Centre for Diffraction Data (ICDD) and the cell parameters were obtained by refinement using Fullprof software [28].

The lamellae prepared from all the samples were characterized by µX-ray diffraction and µX-ray fluorescence at µXAS beamline on the Swiss Light Source (SLS), Paul Scherrer Institut (PSI), Switzerland. The measurement setup is schematically shown in **Fig. 1f**. A synchrotron-based X-ray beam with a high energy of 17.2 keV was passed through the Kirkpatrick-Baez (KB) mirror which was able to focus the beam to a spot size smaller than 1 $\mu m^2$ (1 µm horizontally by 0.5 µm vertically). The lamella of the sample was then positioned at the focal plane and two-dimensional (2D) raster scans on X (horizontal) and Y (vertical) directions were performed all over the lamella using the step size of 500 nm. Since the energy was high, the X-ray was able to transmit through the thin lamella. An area detector positioned behind the lamella and perpendicular to the incident beam was used to record the 2D projections of the diffracted beam. Apart from it, a fluorescence detector was positioned at 90° from the incident beam. Thus, both the local diffraction pattern and fluorescence spectrum can be recorded simultaneously. The diffraction ring of each measured point was azimuthally integrated by utilizing pyFAI, a Python library, to obtain the traditional 1D diffractograms [29]. The 1D diffractograms were then integrated along the horizontal direction parallel to the electrolyte (X-direction in **Fig. 1f**) for each vertical position in the electrode thickness (Y-direction in **Fig. 1f**). Therefore, a set of 1D diffractograms is obtained so that the distribution of the phases across the thickness of the samples can be examined. The Rietveld refinement and fitting of the diffractograms were carried out by XRDUA software [30,31]. For the quantitative analysis of the phases, batch line fitting was carried out also the same software. The identification of the elements from the fluorescence spectra was performed by PyMCA, a Python library [30]. The 2D maps were generated by using Fiji software.

## 3. Results and Discussion

### 3.1. Long-term tests on symmetrical and complete cells under polarization

The long-term tests are conducted on both symmetrical (samples 3 and 5) and complete (sample 4) cells with the objective to investigate the stability behavior of LPNO electrode under polarization. The impedance measurements of both cells taken before and after the tests are presented in Nyquist plots in **Fig. 2**.

Thanks to the 3-electrode configuration for the symmetrical cells, the upper and lower electrodes working respectively in anodic and cathodic polarizations can be measured independently. The Nyquist plots of both electrodes are shown in **Fig. 2a**. It can be noticed that the response of the electrodes is not perfectly symmetric in spite of the identical material and microstructure. This small difference in the initial $R_{pol}$ values can be attributed to artifacts leading to small distortion on the measurement. They are in general related to the positioning of the Ag-wire reference electrode, which should be perfectly placed in the middle of the electrolyte side, and the alignment of the two LPNO electrodes on the electrolyte [32]. After the long-term test, it is observed that both electrodes have different behavior in either electrolysis or fuel cell modes as indicated by the significant different evolutions in the $R_{pol}$ values. The response of the anodic side (operated in electrolysis mode) is almost similar before and after the test for 960 h. Meanwhile, the $R_{pol}$ of the cathodic side significantly increases to triple the initial value before the test. This result is in agreement with another study on the lanthanum-praseodymium nickelates in which a significant increase (between 4 times for $La_{1.5}Pr_{0.5}NiO_{4+\delta}$ up to 35 times for $Pr_2NiO_{4+\delta}$) of $R_{pol}$ was observed on the electrode operated in fuel cell mode whereas the performance was quite stable in electrolysis mode [13]. Indeed, the different behavior under electrolysis and fuel cell modes might be caused by different reaction and decomposition processes of LPNO under either anodic or cathodic polarization [33]. The decomposition products under cathodic polarization might be more detrimental on the electrochemical performance of the electrode (e.g. decomposition products that were insulators or could cause delamination), thus the $R_{pol}$ significantly increases after the aging. Some post-mortem characterizations have been carried out to corroborate this proposition which will be detailed in §3.2-3.3.

The long-term test on the complete cell (sample 4) has also been carried out in electrolysis mode. In the Nyquist plots displayed in **Fig. 2b**, the initial $R_{pol}$ is comparably much larger than the initial $R_{pol}$ of the symmetrical cell since it includes more processes with the hydrogen electrode overpotential and the losses due to the gas diffusion in the thick cell support. Nonetheless, it is worth to note that after the long-term test in the electrolysis mode, there are no changes in the $R_{pol}$ of the complete cell nor on each contribution in the spectrum. This observation indicates the response of the cell component including the oxygen electrode is not impacted by the operation in electrolysis mode. This statement is in perfect line with the stability of the electrode of the symmetrical cell when operated under anodic current.
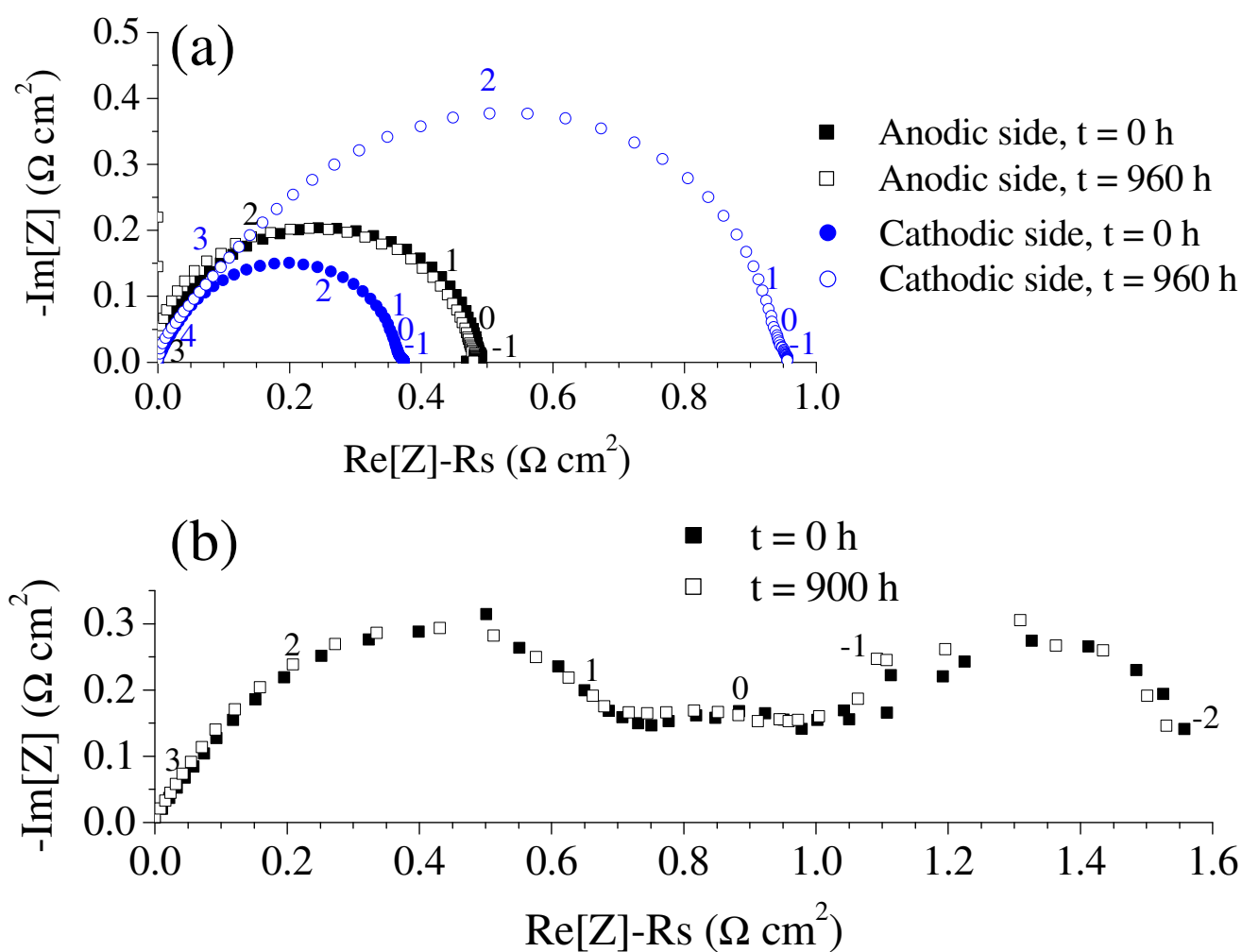
**Fig. 2** The Nyquist plots at 700 °C taken before and after durability tests of (a) sample 3 (anodic side) and sample 5 (cathodic side), and (b) sample 4. The contribution of series resistances is subtracted for easier comparison. The numbers indicate the logarithm of the measuring frequency.

### 3.2. Post-mortem microstructural characterization

 To detect any microstructural changes after the long-term tests, SEM observations have been carried out on the pristine and tested electrodes and some 3D reconstructions have been performed on selected samples.

### 3.2.1 Characterization of the samples operated in the electrolysis mode

The SEM images of the pristine electrode (sample 1), as well as the anodically-aged electrodes in the symmetrical and complete cell configurations (samples 3 and 4), can be viewed in **Fig. S2a, S2b,** and **S2c,** respectively. The 3D rendering volumes for the reconstructions of the pristine cell (sample 1) and anodic side of the symmetrical cell (sample 3) are shown in **Fig. 3a** and **3b**.

From the visual inspection of the SEM images and the 3D reconstructions, no striking microstructure changes can be detected before and after the long-term testing. In addition, good adhesion of LPNO electrode on GDC electrolyte is preserved after the anodic aging. To go further in the analysis and to validate these preliminary observations, the microstructural properties of both sample 1 and sample 3, are then computed from the 3D reconstructions. The data in terms of volume fraction, mean particle diameter, specific surface area, and tortuosity factor are given in **Table 2.** After the long-term test in the electrolysis mode, the porosity in the electrode is almost identical with the fresh sample and there is no obvious particle growth. These statements mean that there is no sign of layer densification. Only a minor decrease in the specific surface area is found. This evolution can be explained by the first stage of the material sintering that occurs at a very low rate. Finally, it can be mentioned that the tortuosity factor is not affected by the operation. All these results indicate that the microstructure is not significantly changed upon operation, which is consistent with the stability of the electrode performance in the electrolysis mode.

### 3.2.2 Characterization of the sample operated in fuel cell mode

In contrast to the sample operated in the electrolysis mode, severe delamination of LPNO electrode appears at the GDC interface after the operation in fuel cell mode (sample 5) as shown in **Fig. 3c**. It is

The detachment could be caused by the formation of phase(s) close to the electrolyte interface with expansion/contraction that could trigger the debonding. To justify this hypothesis, further structural characterization of the cathodic side will be discussed in §3.3.4. Nevertheless, it can be pointed out that the significant increase of the $R_{pol}$ for the sample aged in fuel cell mode must be largely attributed to the electrode delamination.
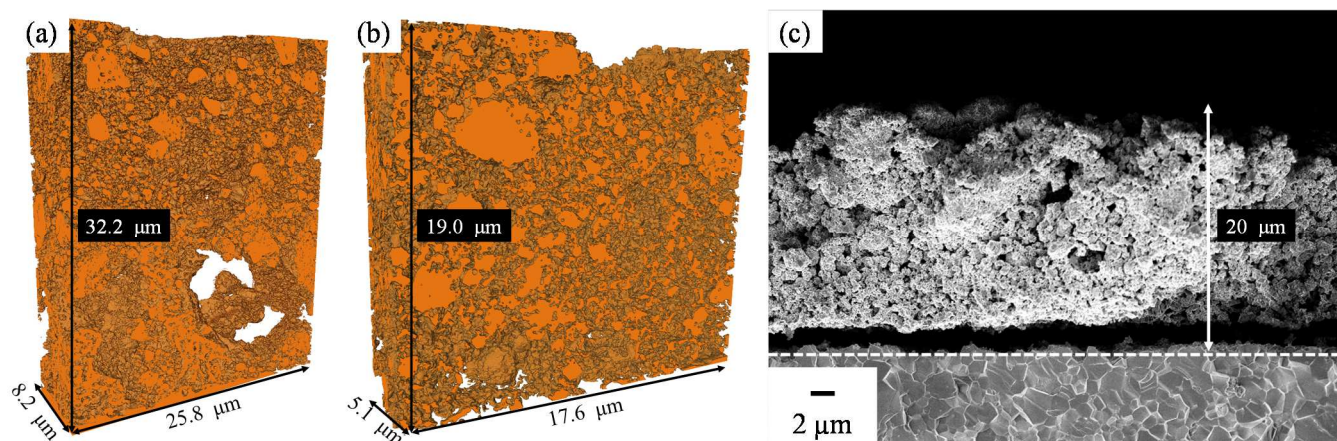


**Fig. 3** The 3D reconstruction visualization of (a) sample 1 and (b) sample 3, as well as (c) the cross-section SEM image of sample 5.

**Table 2** The values of several microstructural properties of the pristine cell and anodic side of the symmetrical cell calculated based on the 3D reconstruction by FIB-SEM.

|  | Porosity (%) | Mean particle diameter (µm) | Specific surface area (µm$^{-1}$) | Tortuosity factor (-) |
|---|---|---|---|---|
| Sample 1 | 59.02 | 0.2170 | 1.8604 | 1.6878 |

| | | | | |
|---|---|---|---|---|
| Sample 3 | 63.06 | 0.1812 | 1.6998 | 1.4938 |

## 3.3. Post-mortem structural characterization

### 3.3.1 Pristine cell

The pristine cell (sample 1) is characterized by both laboratory XRD and synchrotron μ-XRD – μ-XRF. The purpose is to check the LPNO purity in the fresh electrode and to analyze the distribution of any secondary phases in the thickness of the deposit. Since the electrode was in a double-layer configuration, the laboratory XRD characterization is performed separately for both ESD (**Fig. S3a**) and SP layers (**Fig. S3b**). Indeed, X-ray diffraction data obtained in the typical Bragg-Brentano geometry gives a spectral signature throughout the electrode thickness. Thus, it is not possible to differentiate between diffraction patterns from the ESD and SP layers.

As expected, a large quantity of the LPNO phase is detected in the ESD single layer. The phase is indexed to an orthorhombic unit cell with the *Bmab* space group (No. 64). The cell lattice parameters deduced from the Rietveld refinement (a = 5. 432(2) Å, b = 5.475(8) Å, and c = 12.586(9) Å) are found to be in a good agreement with literature data [11]. X-ray diffraction from the GDC electrolyte shows distinct and sharp peaks belonging to cubic unit cell ($Fm\bar{3}m$, No. 225) with a lattice parameter of 5.419(1) Å. This result is also fully consistent with the reported GDC structure (PDF card no 04-002-6160). Apart from LPNO and GDC, there is an apparent presence of a secondary phase which is identified as the higher-order Ruddlesden-Popper phase $(La,Pr)_3Ni_2O_{7-\delta}$, (LP)3N2. The formation of this secondary phase is caused by the decomposition of the LPNO structure which might be due to the small particle size in the ESD layer (130 nm on average) with a coral-like microstructure exhibiting large porosity and large specific surface area (see **Fig. S4a**). In contrast to the ESD film, only the unique LPNO phase without secondary phases is detected in the SP layer. The denser and coarser microstructure of the SP layer (**Fig.**

**S4b**) should explain the higher stability of LPNO phase compared to the very fine microstructure deposited by ESD.

A double-layer pristine electrode is also characterized by μ-XRD and μ-XRF in order to have information on the distribution of the phases in the total volume of the electrode. **Fig. 4a** shows the averaged X-ray diffraction patterns for several vertical positions in the sample (Y-direction) starting from the LPNO/GDC interface. In addition to LPNO, the high-order (LP)3N2 phase is clearly detected at few micrometers above the LPNO/GDC interface (**Fig. 4c**) which corresponds to the ESD layer. Meanwhile, this phase is not observed in the upper region of the electrode related to the SP layer (**Fig. 4b**). These local characterizations are in a good agreement with the result from the laboratory XRD described previously. However, the presence of a supplementary phase, which is not detected by the laboratory XRD, is observed all over the electrode thickness. From the peak refinement (**Fig. 4b** and **4c**), this phase is identified as $Pr_6O_{11}$. There are two main possibilities to explain the detection of this phase only in the synchrotron μ-XRD pattern. The presence of this new phase could be due to a decomposition of the electrode material during the preparation of the lamella. However, this explanation is rather unlikely since there was no clear evidence that the lamella preparation could induce the decomposition of LPNO (from our previous experiments [26]). Alternatively, it is worth noting that the peak intensities corresponding to this phase are very small in such a way that they could be concealed by the peaks of another phase(s) in the laboratory XRD pattern. Indeed, the main $Pr_6O_{11}$ peak (2θ angle of 12.98° by synchrotron beam or 27.98° by Cu-Kα beam) is located very close to GDC peak (2θ angle of 13.22° by synchrotron beam or 28.51° by Cu-Kα beam). Therefore, with the laboratory XRD, the $Pr_6O_{11}$ peak could be completely convoluted by the strong peak intensity coming from the GDC electrolyte.

It can be noticed that $Pr_6O_{11}$ is also an MIEC compound with a very high electronic and ionic conductivity through the electron hopping between the mixed metal oxidation state and high oxygen mobility due to the large concentration of ordered oxygen vacancies [34-36]. A previous study has also shown that this material exhibits a very high electrochemical activity for oxygen oxidation/reduction [37].

Thus, albeit unexpected, the presence of $Pr_6O_{11}$ in the two layers of the electrode must promote the electrochemical processes leading to the improvement of the electrode performances.

The 2D XRD and XRF maps show the distribution of both crystallographic phases and chemical elements in the whole electrode cross-section (**Fig. 5a** and **S5a**). The visualization inspection confirms that the formation of high order phase (LP)3N2 is restricted to the ESD layer whereas the praseodymium oxide $Pr_6O_{11}$ is found on both layers of the electrode. Finally, the observation all along the electrode/electrolyte interface reveals no sign of reactivity between LPNO and GDC.
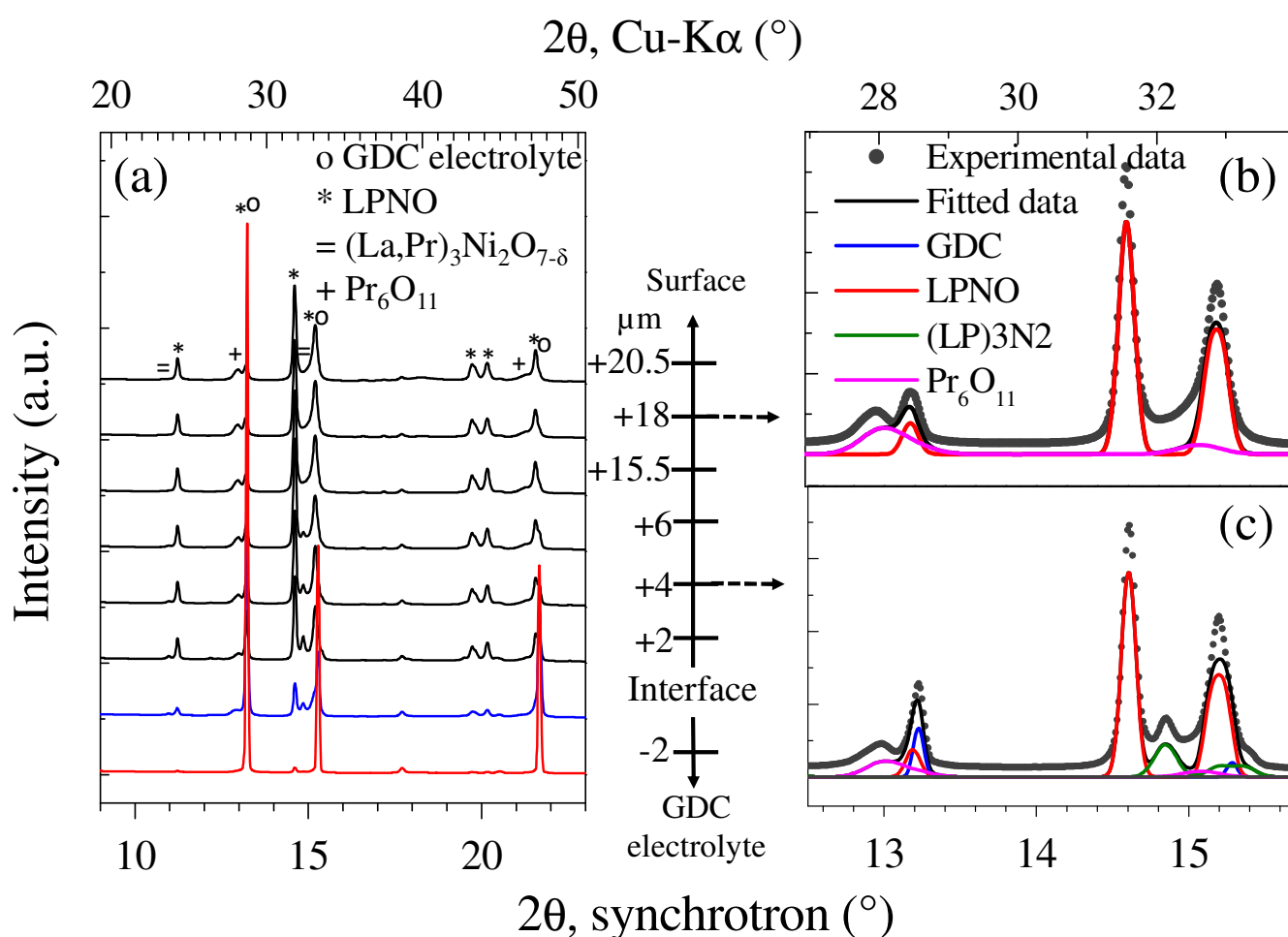


**Fig. 4** (a) The average XRD patterns on several Y-positions and (b)-(c) refinement of the peaks at two different Y-positions, *i. e.* 18 and 4 μm above the electrode/GDC, respectively, for sample 1.
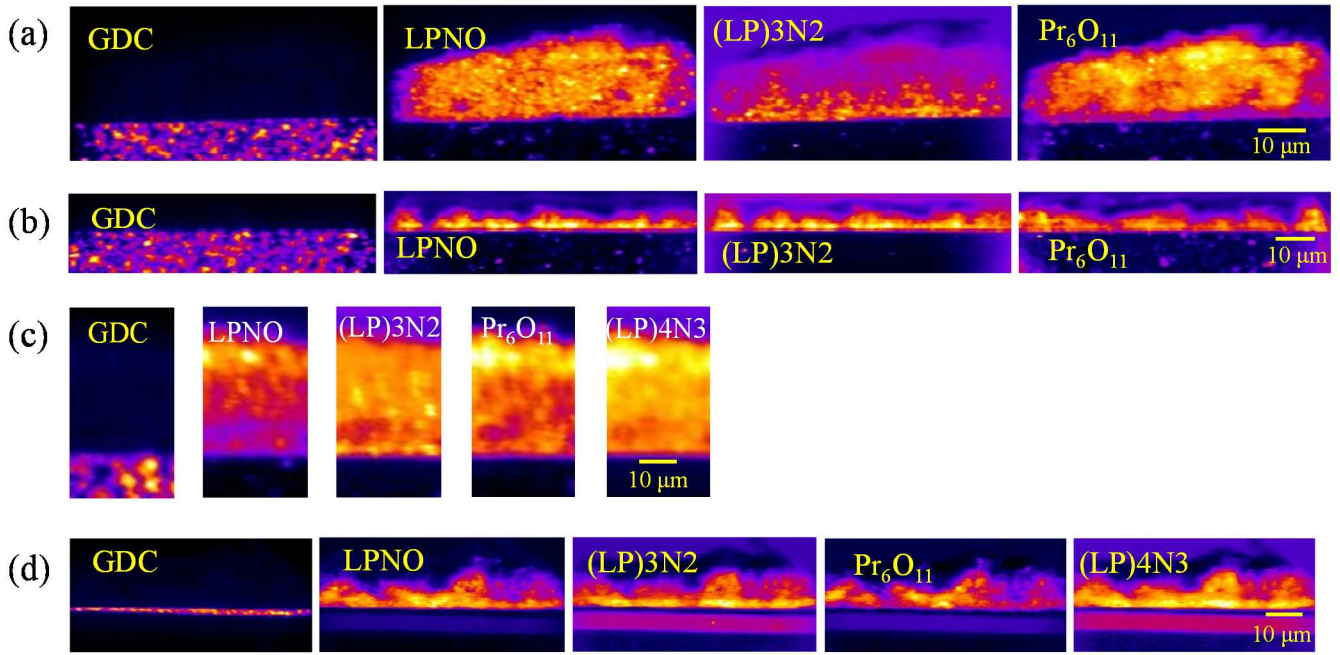
**Fig. 5** 2D maps of the XRD which show the distribution of the phases, namely GDC, LPNO, (LP)3N2, $Pr_6O_{11}$, and (LP)4N3, in (a) sample 1, (b) sample 2, (c) sample 3, and (d) sample 4. The brighter color indicates the higher local intensity of the corresponding compound. The size of the maps for each sample is different due to the variation on the size of the lamella, which is related to the dimension of the electrode itself.
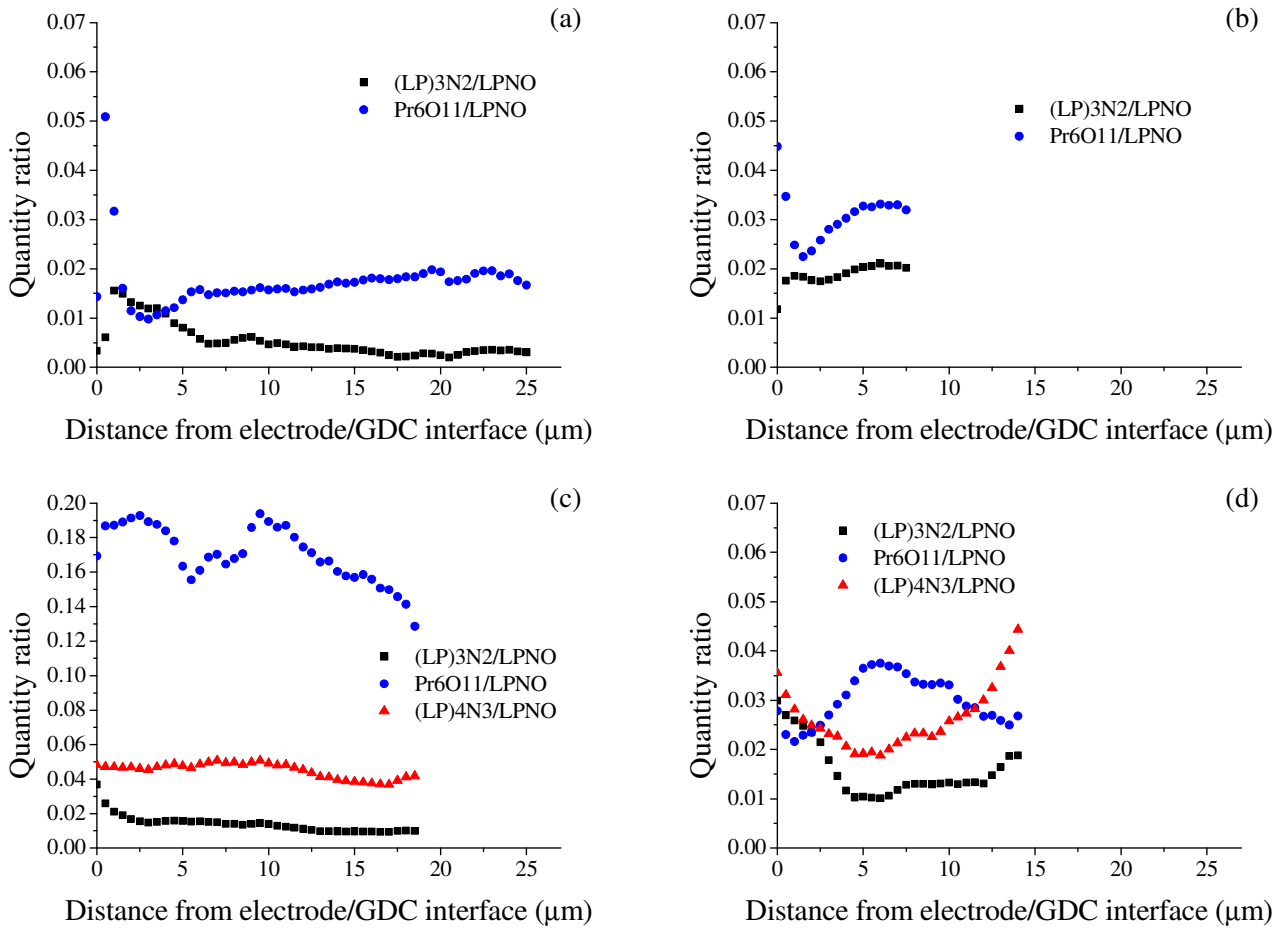
**Fig. 6** The quantitative comparison of (LP)3N2, $Pr_6O_{11}$, and (LP)4N3 to LPNO in the LPNO electrode as the function of distance from electrode/GDC interface for (a) sample 1, (b) sample 2, (c) sample 3, and (d) sample 4.

### 3.3.2 Thermally-aged cell

The thermally-aged cell (sample 2) composed of a single ESD layer deposited on the GDC electrolyte is annealed at 700 °C for 1000 h in air. This durability experiment is conducted only on the ESD layer to check whether the small amount of secondary phases in the fresh material could evolve and would have any impact on the thermal stability of the electrode. From the XRD characterization (**Fig. S6**), it is shown that the thermal aging does not induce the formation of new phases as compared to the ESD layer of the pristine cell. As in the pristine cell, there is also no indication of reactivity between LPNO electrode and

GDC electrolyte as evidently shown in the 2D maps (**Fig. 5b** and **S5b**). However, from the phase quantification from the μ-XRD fitting shown in **Fig. 6a** and **6b**, it seems that the amount of both (LP)3N2 and, especially, $Pr_6O_{11}$ slightly increases after the thermal aging. Therefore, although there are no new decomposition products, the LPNO might slightly decompose into (LP)3N2 and $Pr_6O_{11}$ at 700°C under air.

### 3.3.3 Long-term test in electrolysis mode (anodic polarization): symmetrical and complete cells

Thanks to the μ-XRD characterizations, a new phase is detected on the anodic side of the symmetrical cell (sample 3) after the durability experiment. As shown in **Fig. 5c** and **7a-c**, this new phase is found to appear on both ESD and SP layers. The peak refinement (**Fig. 7b** and **7c**) has allowed identifying this compound as another higher-order Ruddlesden-Popper phase $(La,Pr)_4Ni_3O_{10-\delta}$, abbreviated as (LP)4N3. Moreover, the phase of (LP)3N2 was also found in the SP layer which previously was not present in the SP layer of the pristine cell. Additionally, the phase quantification unambiguously shows that the amount of $Pr_6O_{11}$ is significantly higher after aging (**Fig. 6c**). From all these results, it can be concluded that the operation in electrolysis mode accelerates the decomposition of LPNO compared to simple thermal aging. Nevertheless, all these phases including (LP)4N3 are known to be electrochemically active [20,38]. Besides, according to the 2D maps of crystalline phases and chemical elements (**Fig. 5c** and **S5c**), no reactivity is detected after operation between LPNO electrode and GDC electrolyte. For these reasons, the electrode response should not be affected by the aging, which is consistent with the electrode performance stability measured in electrolysis mode (see §3.1).
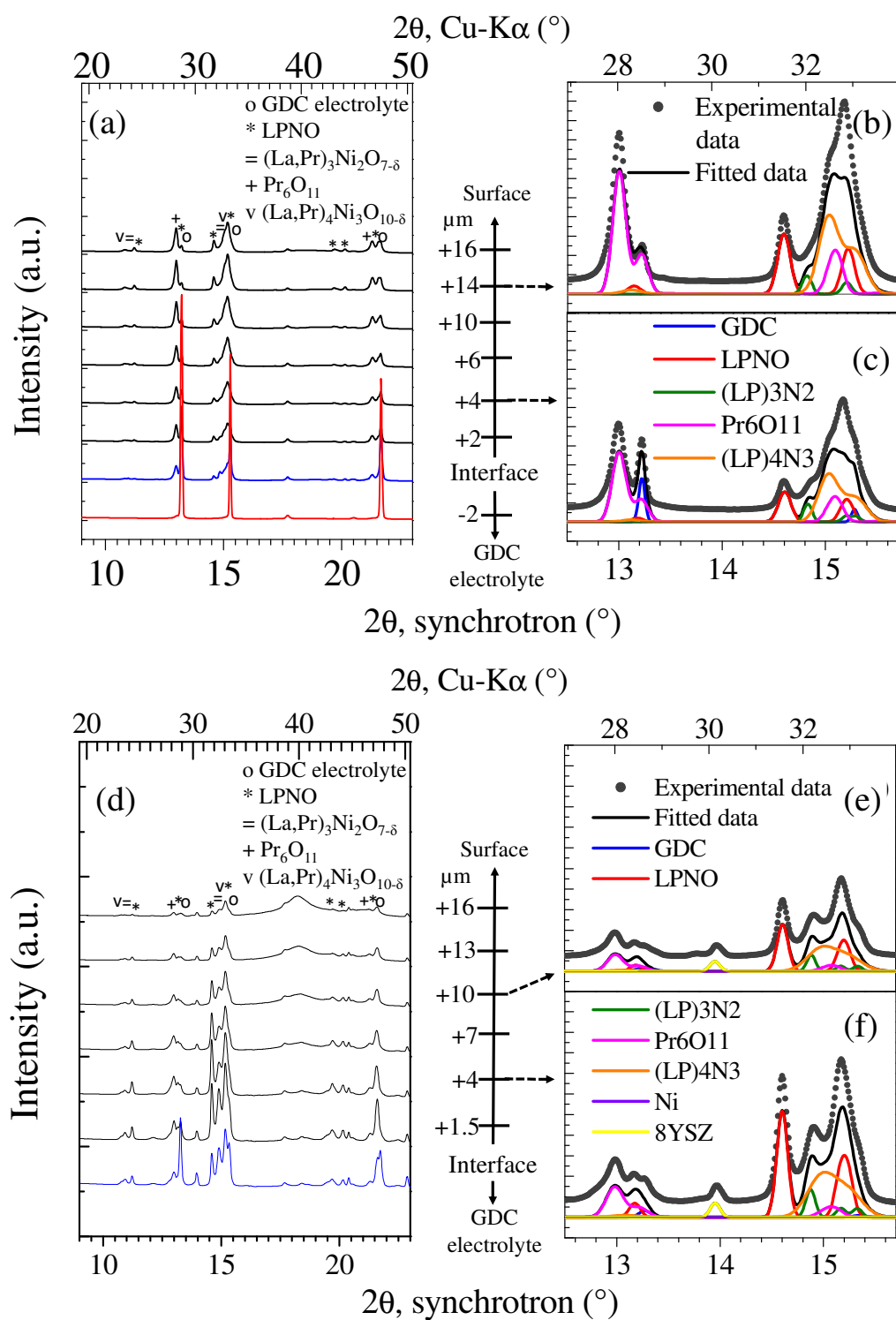
**Fig. 7** (a) The average XRD patterns on several Y-positions and (b)-(c) refinement of the peaks at two different Y-positions, *i. e.* 14 and 4 μm above the electrode/GDC interface, respectively, for sample 3. (d) The average XRD patterns on several Y-positions and (e)-(f) refinement of the peaks at two different Y-positions, *i. e.* 10 and 4 μm above the electrode/GDC interface, respectively, for sample 4.

The µ-XRD characterization data on the LPNO electrode of the complete cell (sample 4) after long-term test in electrolysis mode shows that the final phases are similar to the anodic side of the symmetrical cell (sample 3). Indeed, (LP)4N3 is also formed in both ESD and SP layer while the decomposition in (LP)3N2 extends in the SP layer (**Fig. 5d** and **7d-f**). These observations reinforce the statement that the operation in electrolysis mode favors the LPNO destabilization. However, conversely to the symmetrical cell, the quantifications have shown that the amount of $Pr_6O_{11}$ seems to be not really increased after operation. This apparent discrepancy between the two samples can be explained by the difference in aging condition. Indeed, the durability test with the symmetrical cell was performed at higher current than for the complete cell (anodic current of +300 mA $cm^{-2}$ vs +200 mA $cm^{-2}$). From this point of view, the underlying mechanisms accelerating the material destabilization under electrolysis mode should be related to the current or the electrode overpotential. In this frame, it could be suggested that the change of the LPNO oxygen stoichiometry under electrolysis current could favor the decomposition.

Finally, the 2D maps for the complete cell show that there is no indication of reaction between LPNO and GDC. However, a composition gradient of Ce and Gd is detected in the GDC barrier layer (**Fig. S5d**). The area close to LPNO electrode is richer in Ce while the area close to the 8YSZ electrolyte is richer in Gd. However, it is still not clear whether the origin of this gradient of composition was from the fabrication of the half-cell itself or from the durability test.

### 3.3.4 Long-term test in fuel cell mode (cathodic polarization): symmetrical cell

Because of difficulties in the specimen preparation due to the poor electrode attachment onto the electrolyte after aging in fuel cell mode, only laboratory XRD characterizations are carried out on sample 5. Indeed, the electrode aged under cathodic polarization was delaminated in such a way that the thin lamella were lost during the last stage of the preparation (cf. Fig. 1). Even if the laboratory XRD technique cannot provide information within the thickness of the electrode, the presence or appearance of

secondary phases after the long-term operation can be compared to the pristine cell. As for the electrode aged in the electrolysis mode, the secondary phases (LP)3N2, $Pr_6O_{11}$, and (LP)4N3 have also been detected in sample 5 (**Fig. 8b**). Conversely to the pristine electrode (**Fig. 8a**), it can be noticed that the possibility to detect the $Pr_6O_{11}$ phase with laboratory equipment for the aged sample proves that its quantity has been significantly increased. These results suggest that the cathodic current also accelerates the LPNO destabilization. However, at this stage, it still unclear whether the decomposition is more pronounced when the electrode is operated in fuel cell or electrolysis mode. Moreover, this structural characterization does not reveal a strong reactivity at the electrode/GDC interface that could explain the delamination. Therefore, it can be speculated that the amount of the secondary phases formed under fuel cell current is higher so that they could destabilize the interface. In addition, one could consider another origin of LPNO degradation coming from the mechanism of the oxygen reduction reaction that occurs at the cathodic side in fuel cell mode. Indeed, in these reducing conditions under cathodic polarization, the oxygen overstoichiometry in $LaPrNiO_{4+\delta}$ material is decreased since a flux of oxide ions are transported from the cathode to the anode through the electrolyte. The LPNO is consequently losing some interstitial oxygen ions and this evolution should not be in favour of its structural stability. On the contrary, when LPNO is working as an anode material in oxidizing conditions in the electrolysis mode, LPNO is fed by oxygen ions that could occupy interstitial sites of the structure. Therefore, the increase of the oxygen overstoichiometry under anodic current could be less impacting and could limit the LPNO structural instability compared to an operation under cathodic current. On the contrary for materials exhibiting oxygen understoichiometry such as the state-of-the-art Lanthanum Strontium Cobalt Ferrite (LSCF) electrodes, it is interesting to note that the performance degradation caused by either delamination or cation diffusion and the formation of secondary phase had been observed during the practical operation in electrolysis mode [39-41]. Moreover, in a present review work [33], the authors focus on providing an understanding of SOEC degradation in which the role of oxygen chemical activity appears as a major factor governing various degradation phenomena including cation diffusion, secondary phase formation,

and delamination of the electrode. Finally, in the specific case of LPNO electrode, the delamination could also be related to the behavior of $Pr_6O_{11}$ in different $pO_2$. As mentioned in the literature [42,43], a phase transition of praseodymium oxide ($PrO_x$) from $Pr_6O_{11}$ (=$PrO_{1.83}$) to $Pr_7O_{12}$ (=$PrO_{1.71}$) appears at either ~700 °C in air or in a slightly low $pO_2$ environment, or at ~800 °C in high $pO_2$. Since the test in SOFC mode is carried out at 700 °C, this structural transition could take place in the vicinity of the interface where low $pO_2$ is induced by the reaction of oxygen reduction.
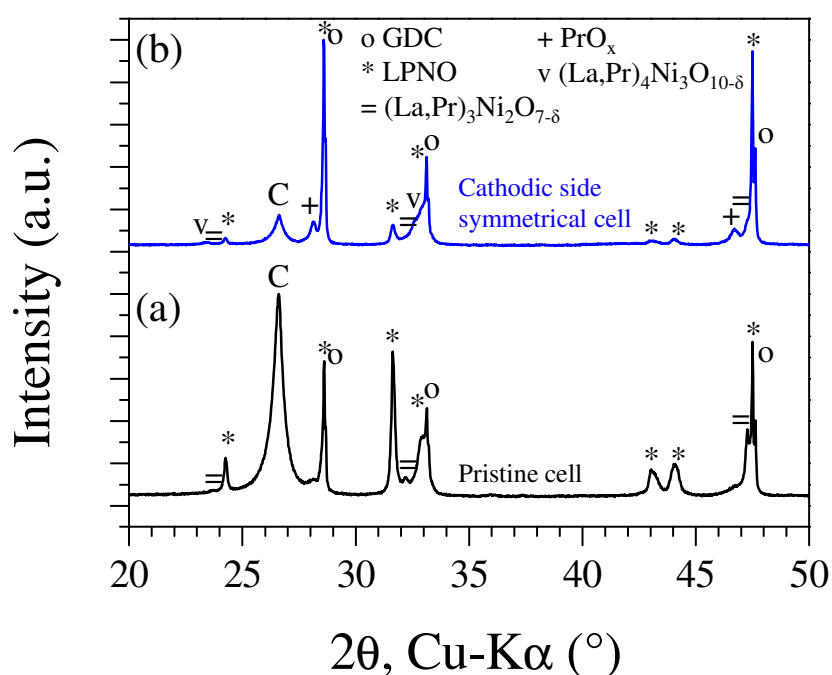


**Fig. 8** The lab XRD of sample 1 (a) and sample 5 (b). The symbol 'C' indicated the carbon phase which is originating from the carbon tape used for sample preparation by p-FIB.

## 4. Conclusions

In this work, a comprehensive durability study of LPNO electrode prepared by ESD and SP has been reported for the first time. Long-term tests have been conducted on both symmetrical and complete cells under current at 700 °C for ≈1000 h. To unravel the impact of temperature and polarization, a single ESD

layer was thermally-aged in the same conditions. The durability experiments have shown that the polarization resistance ($R_{pol}$) of the electrode did not change after the test in electrolysis mode for both symmetrical and complete cells while a significant increase was observed under fuel cell mode (symmetrical cell). Several microstructural and structural characterizations were then performed to investigate the behavior of LPNO electrode under polarization. SEM observations and FIB-SEM reconstructions have shown that the microstructure is not affected by the operation. However, the sample aged in fuel cell mode exhibits severe delamination at the electrode/electrolyte interface which is not observed for the electrode operating in the electrolysis mode. This delamination at the LPNO/GDC interface must explain the higher degradation rate induced by the fuel cell operation.

In complementarity of the microstructural analysis, structural characterizations by laboratory XRD and synchrotron μ-XRD and μ-XRF have been performed. For the pristine electrode analyzed just after the manufacturing process, it has been found that the fine microstructure of the ESD layer induces a minor decomposition into the (LP)3N2 and $Pr_6O_{11}$ secondary phases while the coarse microstructure of the SP layer is more stable with only the presence of $Pr_6O_{11}$. It can be noticed that the amount of this phase is very limited in the pristine samples in such a way that it can be only detected in the μ-XRD pattern.

The structural observation for the thermally-aged electrode has not revealed the formation of any additional secondary phases. However, a slight increase in the amount of (LP)3N2 and, especially $Pr_6O_{11}$, has been detected indicating that LPNO in the ESD layer is decomposed at a very slow rate in temperature.

Compared to the thermal aging, it has been found that the LPNO decomposition is much more pronounced for the electrodes operated in an anodic or cathodic polarization. Indeed, for the samples aged in the electrolysis mode, the μ-XRD maps have shown that a new secondary phase (LP)4N3 appears in both the ESD and SP layers. Moreover, the quantity of $Pr_6O_{11}$ is strongly increased especially at high current density, while the formation of (LP)3N2 extends in the SP layer. These results mean that the

operation under electrolysis current accelerates the decomposition of LPNO compared to simple thermal aging. With the XRD laboratory characterizations, the same conclusions have been drawn for the electrode operated in fuel cell modes. However, the difference in the material stability between the two operating modes is still unclear and further investigations are required. Nevertheless, two main hypotheses have been proposed to account for the electrode delamination only observed in fuel cell mode. Firstly, since the oxygen overstoichiometry decreases under cathodic current, especially at the electrolyte interface where the depletion in interstitial oxygen should be the highest, the rate of the LPNO destabilization could be accelerated compared to the anodic operation. Secondly, the behavior of $Pr_6O_{11}$ under reducing atmosphere at the electrolyte interface in fuel cell condition could also participate or explain the delamination.

To conclude, the suitability of LPNO as a durable oxygen electrode for electrolysis cell has been proved to be promising. Indeed, the electrode polarization resistances of the complete cell remain unchanged after the durability test carried out under electrolysis current thanks to the presence of electrochemically active secondary phases coming from the decomposition of the LPNO phases.

**References:**

[1]     S.P.S. Badwal, S. Giddey, C. Munnings, A. Kulkarni, Review of progress in high temperature solid oxide fuel cells, J. Aust. Ceram. Soc. 50 (2014) 23–37.

[2]     N. Mahato, A. Banerjee, A. Gupta, S. Omar, K. Balani, Progress in material selection for solid oxide fuel cell technology: A review, Prog. Mater. Sci. 72 (2015) 141–337. https://doi.org/10.1016/j.pmatsci.2015.01.001.

[3]     E.D. Wachsman, K.T. Lee, Lowering the temperature of solid oxide fuel cells, Sci. 334 (2011) 935–940. https://doi.org/10.1126/science.1204090.

[4]     D.J.L. Brett, A. Atkinson, N.P. Brandon, S.J. Skinner, Intermediate temperature solid oxide fuel cells, Chem. Soc. Rev. 37 (2008) 1568–1578. https://doi.org/10.1039/b612060c.

[5]     A. Tarancón, S.J. Skinner, R.J. Chater, F. Hernández-Ramírez, J.A. Kilner, Layered perovskites as promising cathodes for intermediate temperature solid oxide fuel cells, J. Mater. Chem. 17 (2007) 3175–3181. https://doi.org/10.1039/b704320a.

[6]     A. Chroneos, D. Parfitt, J.A. Kilner, R.W. Grimes, Anisotropic oxygen diffusion in tetragonal La2NiO4+$\delta$: Molecular dynamics calculations, J. Mater. Chem. 20 (2010) 266–270. https://doi.org/10.1039/b917118e.

[7]     E. Boehm, J.M. Bassat, P. Dordor, F. Mauvy, J.C. Grenier, P. Stevens, Oxygen diffusion and transport properties in non-stoichiometric Ln2-xNiO4+$\delta$ oxides, Solid State Ionics. 176 (2005) 2717–2725. https://doi.org/10.1016/j.ssi.2005.06.033.

[8]     J.M. Bassat, P. Odier, J.P. Loup, The semiconductor-to-metal transition in question in La$_{2-x}$NiO$_{4+\delta}$ ($\delta$ > 0 or $\delta$ < 0), J. Solid State Chem. 110 (1994) 124-135. https://doi.org/10.1006/jssc.1994.1146.

[9]     S.J. Skinner, J.A. Kilner, Oxygen diffusion and surface exchange in La$_{2-x}$Sr$_x$NiO$_{4+\delta}$, Solid State Ionics. 135 (2000) 709–712. https://doi.org/10.1016/S0167-2738(00)00388-X.

[10]    A. Tarancón, M. Burriel, J. Santiso, S.J. Skinner, J.A. Kilner, Advances in layered oxide cathodes for intermediate temperature solid oxide fuel cells, J. Mater. Chem. 20 (2010) 3799-3813. https://doi.org/10.1039/b922430k.

[11]   V. Vibhu, A. Rougier, C. Nicollet, A. Flura, J.C. Grenier, J.M. Bassat, La2-xPrxNiO4+δ as suitable cathodes for metal supported SOFCs, Solid State Ionics. 278 (2015) 32–37. https://doi.org/10.1016/j.ssi.2015.05.005.

[12]   A. Montenegro-Hernández, J. Vega-Castillo, L. Mogni, A. Caneiro, Thermal stability of Ln2NiO4+δ (Ln: La, Pr, Nd) and their chemical compatibility with YSZ and CGO solid electrolytes, Int. J. Hydrogen Energy. 36 (2011) 15704–15714. https://doi.org/10.1016/j.ijhydene.2011.08.105.

[13]   V. Vibhu, J.-M. Bassat, A. Flura, C. Nicollet, J.-C. Grenier, A. Rougier, Influence of La/Pr Ratio on the Ageing Properties of La2-XPrxNiO4+δ as Cathodes in IT-SOFCs, ECS Trans. 68 (2015) 825–835. https://doi.org/10.1149/06801.0825ecst.

[14]   R.K. Sharma, S.-K. Cheah, M. Burriel, L. Dessemond, J.-M. Bassat, E. Djurado, Design of La2−xPrxNiO4+δ SOFC cathodes: a compromise between electrochemical performance and thermodynamic stability, J. Mater. Chem. A. 5 (2017) 1120–1132. https://doi.org/10.1039/C6TA08011A.

[15]   N.I. Khamidy, J. Laurencin, E. Djurado, Improving the electrochemical performance of LaPrNiO4+δ as an oxygen electrode for intermediate temperature solid oxide cells by varying the architectural design, J. Electroanal. Chem. 849 (2019) 113373. https://doi.org/10.1016/j.jelechem.2019.113373.

[16]   O. Çelikbilek, D. Jauffres, E. Siebert, L. Dessemond, M. Burriel, C. L. Martin, E. Djurado, Rational design of hierarchically nanostructured electrodes for solid oxide fuel cells, J. Power Sources 333 (2016) 72-82. https://doi.org/10.1016/j.jpowsour.2016.09.156.

[17]   E. Effori, H. Moussaoui, F. Monaco, R.K. Sharma, J. Debayle, Y. Gavet, G. Delette, G. Si Larbi, E. Siebert, J. Vulliet, L. Dessemond, J. Laurencin, Reaction Mechanism and Impact of

Microstructure on Performances for the LSCF-CGO Composite Electrode in Solid Oxide Cells, Fuel Cells 19 No. 4 (2019) 429–444. https://doi.org/10.1002/fuce.201800185.

[18]  A. Hauch, K. Brodersen, M. Chen, and M. B. Mogensen, Ni/YSZ electrodes structures optimized for increased electrolysisperformance and durability, Solid State Ionics 293 (2016) 27-36. https://doi.org/10.1016/j.ssi.2016.06.003.

[19]  F. Monaco, M. Hubert, J. Vulliet, J.P. Ouweltjes, D. Montinaro, P. Cloetens, P. Piccardo, F. Lefebvre-Joud, J. Laurencin, Degradation of Ni-YSZ Electrodes in Solid Oxide Cells: Impact of Polarization and Initial Microstructure on the Ni Evolution, J. Electrochem. Soc. 166 (2019) F1229-F1242. https://doi.org/10.1149/2.1261915jes.

[20]  S. Takahashi, S. Nishimoto, M. Matsuda, M. Miyake, Electrode properties of the ruddlesden-popper series, Lan +1NinO3n+1 (n=1, 2, and 3), as intermediate-temperature solid oxide fuel cells, J. Am. Ceram. Soc. 93 (2010) 2329–2333. https://doi.org/10.1111/j.1551-2916.2010.03743.x.

[21]  Z. Lou, J. Peng, N. Dai, J. Qiao, Y. Yan, Z. Wang, J. Wang, K. Sun, High performance La3Ni2O7 cathode prepared by a facile sol-gel method for intermediate temperature solid oxide fuel cells, Electrochem. Commun. 22 (2012) 97–100. https://doi.org/10.1016/j.elecom.2012.06.004.

[22]  J.C. Park, D.K. Kim, S.H. Byeon, D. Kim, XANES study on Ruddlesden-Popper phase, Lan+1NinO3n+1 (n = 1, 2 and ∞), J. Synchrotron Radiat. 8 (2001) 704–706. https://doi.org/10.1107/S0909049500015983.

[23]  C.H. Chen, E.M. Kelder, M.J.G. Jak, J. Schoonman, Electrostatic spray deposition of thin layers of cathode materials for lithium battery, Solid State Ionics. 86–88 (1996) 1301–1306. https://doi.org/10.1016/0167-2738(96)00305-0.

[24]  R.K. Sharma, M. Burriel, L. Dessemond, V. Martin, J.M. Bassat, E. Djurado, An innovative

architectural design to enhance the electrochemical performance of La2NiO4+?? cathodes for solid oxide fuel cell applications, J. Power Sources. 316 (2016) 17–28. https://doi.org/10.1016/j.jpowsour.2016.03.067.

[25] H. Moussaoui, J. Laurencin, Y. Gavet, G. Delette, M. Hubert, P. Cloetens, T. Le Bihan, J. Debayle, Stochastic geometrical modeling of solid oxide cells electrodes validated on 3D reconstructions, Comput. Mater. Sci. 143 (2018) 262–276. https://doi.org/10.1016/j.commatsci.2017.11.015.

[26] M. Hubert, J. Laurencin, P. Cloetens, J.C. da Silva, F. Lefebvre-Joud, P. Bleuet, A. Nakajo, E. Siebert, Role of microstructure on electrode operating mechanisms for mixed ionic electronic conductors: From synchrotron-based 3D reconstruction to electrochemical modeling, Solid State Ionics. 294 (2016) 90–107. https://doi.org/10.1016/j.ssi.2016.07.001.

[27] T. Tao, Focused ion beam induced deposition of platinum, J. Vac. Sci. Technol. B. 8 (1990) 1826. https://doi.org/10.1116/1.585167.

[28] J. Rodríguez-Carvajal, Recent advances in magnetic structure determination by neutron powder diffraction, Phys. B. 192 (1993) 55–69. https://doi.org/10.1016/0921-4526(93)90108-I.

[29] G. Ashiotis, A. Deschildre, Z. Nawaz, J.P. Wright, D. Karkoulis, F.E. Picca, J. Kieffer, The fast azimuthal integration Python library: pyFAI, J. Appl. Crystallogr. 48 (2015) 510–519. https://doi.org/10.1107/s1600576715004306.

[30] W. De Nolf, K. Janssens, Micro X-ray diffraction and fluorescence tomography for the study of multilayered automotive paints, Surf. Interface Anal. 42 (2010) 411–418. https://doi.org/10.1002/sia.3125.

[31] W. De Nolf, F. Vanmeert, K. Janssens, XRDUA : crystalline phase distribution maps by two-dimensional scanning and tomographic (micro) X-ray powder diffraction, J. Appl. Crystallogr. 47

(2014) 1107–1117. https://doi.org/10.1107/s1600576714008218.

[32]    M. Cimenti, A.C. Co, V.I. Birss, J.M. Hill, Distortions in electrochemical impedance spectroscopy measurements using 3-electrode methods in SOFC. I-effect of cell geometry, Fuel Cells. 7 (2007) 364–376. https://doi.org/10.1002/fuce.200700019.

[33]    Y. Wang, W. Li, L. Ma, W. Li, X. Liu, Degradation of solid oxide electrolysis cells: phenomena, mechanisms, and emerging mitigation strategies – a review, J. Mater. Sci. Technol. (2019). https://doi.org/10.1016/j.jmst.2019.07.026.

[34]    V. Thangadurai, R.A. Huggins, W. Weppner, Mixed ionic-electronic conductivity in phases in the praseodymium oxide system, J. Solid State Electrochem. 5 (2001) 531–537. https://doi.org/10.1007/s100080000187.

[35]    B.M. Abu-Zied, Y.A. Mohamed, A.M. Asiri, Fabrication, characterization, and electrical conductivity properties of $Pr_6O_{11}$ nanoparticles, J. Rare Earths. 31 (2013) 701–708. https://doi.org/10.1016/S1002-0721(12)60345-7.

[36]    S. Shrestha, C.M.Y. Yeung, C. Nunnerley, S.C. Tsang, Comparison of morphology and electrical conductivity of various thin films containing nano-crystalline praseodymium oxide particles, Sensors Actuators A. 136 (2007) 191–198. https://doi.org/10.1016/j.sna.2006.11.019.

[37]    R.K. Sharma, N.I. Khamidy, L. Rapenne, F. Charlot, H. Moussaoui, J. Laurencin, E. Djurado, Highly efficient architectured $Pr_6O_{11}$ oxygen electrode for solid oxide fuel cell, J. Power Sources. 419 (2019) 171–180. https://doi.org/10.1016/j.jpowsour.2019.02.077.

[38]    R.K. Sharma, M. Burriel, E. Djurado, $La_4Ni_3O_{10-\delta}$ as an efficient solid oxide fuel cell cathode: electrochemical properties versus microstructure, J. Mater. Chem. A. 3 (2015) 23833–23843. https://doi.org/10.1039/C5TA07862H.

[39] J. Laurencin, M. Hubert, D. Ferreira Sanchez, S. Pylypko, M. Morales, A. Morata, B. Morel, D. Montinaro, F. Lefebvre-Joud, E. Siebert, Degradation mechanism of La0.6Sr0.4Co0.2Fe0.8O3-δ/Gd0.1Ce0.9O2-δ composite electrode operated under solid oxide electrolysis and fuel cell conditions, Electrochimica acta, 241 (2017) 459-476. http://dx.doi.org/10.1016/j.electacta.2017.05.011

[40] J. Schefold, A. Brisse, H. Poepke, 23,000 h steam electrolysis with an electrolyte supported solid oxide cell, Int. J. Hydrogen Energy. 42 (2017) 13415-13426. https://doi.org/.10.1016/j.ijhydene.2017.01.072.

[41] F. Tietz, D. Sebold, A. Brisse, J. Schefold, Degradation phenomena in a solid oxide electrolysis cell after 9000 h of operation, J. Power Sources 223 (2013) 129-135. https://doi.org/10.1016/j.jpowsour.2012.09.061.

[42] V. Vibhu, Stability and ageing studies of Praseodymium-based nickelates as cathodes for Solid Oxide Fuel Cells, Université de Bordeaux, 2016.

[43] B.G. Hyde, D.J.M. Bevan, L. Eyring, On the Praseodymium+Oxygen System, Philos. Trans. R. Soc. A. 259 (1966) 583–614. https://doi.org/10.1098/rsta.1966.0025.